Adaptive Optics Scanning Laser Ophthalmoscopy Images in a Family with the Mitochondrial DNA T8993C Mutation

Michael K. Yoon,[1] Austin Roorda,[2] Yuhua Zhang,[2] Chiaki Nakanishi,[1] Lee-Jun C. Wong,[3] Qing Zhang,[3] Leslie Gillum,[4] Ari Green,[4] and Jacque L. Duncan[1]

Purpose. This study was designed to assess the effect of mitochondrial DNA (mtDNA) mutation T8993C on cone structure in a family expressing neurogenic muscle weakness, ataxia, and retinitis pigmentosa (NARP) syndrome.

Methods. Five family members were studied, using clinical examination, nerve conduction studies, perimetry, optical coherence tomography (OCT) measures of central retinal thickness, and electroretinography. High-resolution images of cone structure using adaptive optics scanning laser ophthalmoscopy (AOSLO) were obtained in four subjects with stable fixation. Cone spacing was compared to 18 age-similar normal subjects and converted to *z*-scores at each location where unambiguous cones were identified. Tissue levels of T8993C mutant heteroplasmy in blood and hair follicles were quantified using real-time allele-refractory mutations system (ARMS) quantitative polymerase chain reaction (qPCR).

Results. Subjects expressing the T8993C mutation showed varying levels of disease severity. The subject with the lowest mutant load (42%–54%) showed no neurologic or retinal abnormalities. The remaining four subjects with over 77% mutant load all expressed severe neurologic and/or retinal abnormalities. AOSLO images revealed three patterns of cone spacing: pattern 1, normal; pattern 2, increased cone spacing within a contiguous cone mosaic; and pattern 3, patchy cone loss with increased cone spacing. Visual function was most severely affected in pattern 3.

Conclusions. High levels of T8993C mutant load were associated with severe neurologic or visual dysfunction, while lower levels caused no detectable abnormalities. Visual function was better in patients with a contiguous and regular cone mosaic. Patients expressing high levels of the mtDNA T8993C mutation show abnormal cone structure, suggesting normal mitochondrial DNA is necessary for normal waveguiding by cones. (*Invest Ophthalmol Vis Sci.* 2009;50:1838–1847) DOI:10.1167/iovs.08-2029

Mitochondrial DNA (mtDNA) mutations affect the eye in several ways, causing optic atrophy, progressive external ophthalmoplegia, and retinal degeneration.[1,2] Damaged mtDNA is particularly detrimental to non-dividing cells such as neurons, photoreceptors, and retinal pigment epithelial (RPE) cells, because mutations accumulate without the possibility to lose mutant mtDNA during cell replication.[3] Neurodegeneration and retinal degeneration are often associated with diseases caused by mtDNA mutations.[4] A point mutation at mtDNA nucleotide 8993 in subunit 6 of mitochondrial respiratory chain complex V, ATP synthase, results in neurogenic muscle weakness, ataxia, and retinitis pigmentosa (NARP).[5] Subunit 6 of ATP synthase forms part of the membrane-spanning channel involved in oxidative phosphorylation. Mutations in this gene impair ATP production. The most common mutation is T8993G, which converts a conserved leucine to arginine in the F_o portion of the F_1F_o ATP synthase and alters the electrical charge of the proton channel.[6] In the less common T8993C mutation, proline replaces leucine, which does not alter the electrical charge, but may change the channel conformation to permit ATP synthesis with reduced efficiency.[7] The T8993C mutation results in later onset, slower progression, and less disease severity than the T8993G mutation.[8–10]

Severity of mitochondrial DNA disorders depends on the type of mutation and the amount of mutant mtDNA (mutant load). Mutant mtDNA typically coexists with wild-type mtDNA in affected tissues, known as heteroplasmy.[11] Disease severity is roughly proportional to mutant load in affected tissues. Studies of patients with the T8993G mutation demonstrate that levels of mutant mtDNA >90% result in maternally inherited Leigh syndrome (MILS), a progressive neurodegenerative disorder of infancy that often results in death during the first few years of life, while levels between 70% to 90% produce NARP.[6,8–10,12] However, recent studies have presented significant variation in tissue mutant load and lack of correlation with disease expression.[11,13–16]

NARP usually begins in young adulthood, with neurologic findings such as proximal neurogenic muscle weakness, sensory neuropathy, ataxia, developmental delay, seizures, and dementia.[5] Ocular findings include retinitis pigmentosa,[5] maculopathy, salt and pepper retinopathy,[15] cone dystrophy,[17] and cone-rod dystrophy.[17,18] Reported magnetic resonance image (MRI) findings include cerebral and cerebellar atrophy, and symmetric hyperintense basal ganglia and brain stem lesions.[13,18–20]

The pathogenesis of NARP and other mitochondrial diseases remains largely unknown. However, retinal degeneration

From the Departments of [1]Ophthalmology and [4]Neurology, University of California, San Francisco, California; the [2]School of Optometry, University of California, Berkeley, California; and the [3]Department of Molecular and Human Genetics, Baylor College of Medicine, Houston, Texas.

Supported by a Career Development Award, a Physician Scientist Award, and Unrestricted Grant from Research to Prevent Blindness (JLD); a Career Development Award and a Clinical Center Grant from the Foundation Fighting Blindness (JLD, AR, YZ); NIH-NEI Grants EY00415 (JLD), EY002162 (JLD), and EY014375 (AR); NIH-NCRR Grant KL2RR024130 (AG, LG); That Man May See, Inc. (JLD); The Bernard A. Newcomb Macular Degeneration Fund (JLD); Hope for Vision (JLD); the Karl Kirchgessner Foundation (JLD); and NSF Science and Technology Center for Adaptive Optics, managed by the University of California at Santa Cruz under cooperative agreement #AST-9876783 (AR, YZ).

Submitted for publication March 15, 2008; revised September 11, 2008; accepted February 10, 2009.

Disclosure: **M.K. Yoon**, None; **A. Roorda**, P; **Y. Zhang**, None; **C. Nakanishi**, None; **L.-J.C. Wong**, None; **Q. Zhang**, None; **L. Gillum**, None; **A. Green**, None; **J.L. Duncan**, None

The publication costs of this article were defrayed in part by page charge payment. This article must therefore be marked "*advertisement*" in accordance with 18 U.S.C. §1734 solely to indicate this fact.

Corresponding author: Jacque L. Duncan, Beckman Vision Center, UCSF School of Medicine, 10 Koret Way, Rm. K-129, San Francisco, CA 94143-0730; duncanj@vision.ucsf.edu.

may result from the extremely high metabolic demand of photoreceptors in the context of a mutation that prevents normal ATP synthesis; energy demand may overwhelm supply and cause photoreceptor death. Cone photoreceptor inner segments contain high numbers of mitochondria, to meet metabolic needs or to contribute to inner segment structure.[21–24] A single histopathological study of the retina from a patient with Leigh syndrome and the T8993G mutation demonstrated abnormal, distended mitochondria in RPE cells with overlying absence of macular photoreceptors.[25] There are no histopathological studies of photoreceptor structure from patients with NARP or the T8993C mutation.

It has not been possible to study individual cone photoreceptors affected by mtDNA mutations in living patients because irregularities of the eye's optics limit resolution of retinal images with all methods commonly used.[26] Adaptive optics can compensate for optical aberrations and improve the resolution of retinal images in normal eyes and patients with inherited retinal degenerations.[27–38] In vivo studies of cones on a microscopic scale provide a unique opportunity to analyze the effects of mitochondrial mutations on photoreceptors.

We have characterized the retinal and neurologic phenotype in a family with the T8993C mutation. We address the major challenge limiting understanding of neurodegenerative diseases, the inability to study individual cells during degeneration in living humans, using an adaptive optics scanning laser ophthalmoscope (AOSLO) to obtain single-cell resolution images of macular cones. This non-invasive approach permits correlation between cone structure and function in patients with retinal degeneration caused by the T8993C mutation.

METHODS

Research procedures were performed in accordance with the Declaration of Helsinki. The study protocol was approved by the UCSF and UC Berkeley institutional review boards. All subjects (five women—a mother with all four of her children) gave written informed consent before participation in any of the studies.

Clinical Examination

A complete history was obtained, including information about all known family members. All subjects in the family who were available underwent a complete neurologic examination. Electrophysiological studies performed included conventional nerve testing and electromyography. Clinical findings are summarized in Tables 1 and 2. Measurement of best-corrected visual acuity (BCVA) was performed using a standard eye chart according to the Early Treatment of Diabetic Retinopathy Study (ETDRS) protocol. The eye with better visual acuity and/or more stable fixation was chosen for further study. Goldmann kinetic perimetry was performed with V-4e and I-4e targets. Automated perimetry was completed with a visual field perimeter (Humphrey Visual Field Analyzer; HFA II 750-6116-12.6; Carl Zeiss Meditec, Inc., Dublin, CA) and a system threshold protocol (10-2 SITA Standard; Carl Zeiss Meditec, Inc.) with measurement of foveal thresholds using a Goldmann III stimulus on a white background (31.5 asb); exposure duration was 200 ms. Color vision was tested using a Farnsworth D-15 panel followed by the Lanthony 15-hue desaturated panel in subjects without crossing errors on the Farnsworth D-15 panel. Pupils were dilated with 1% tropicamide and 2.5% phenylephrine before optical coherence tomography (OCT) images were obtained with a laser scanning camera (Spectralis HRA + OCT Laser Scanning Camera System; Heidelberg Engineering, Vista, CA). The infrared beam of the superluminescent diode (average wavelength, 870 nm) was used to acquire 20° horizontal scans through the anatomic fovea. A full-field ERG was performed after 45 minutes of dark adaptation with a Burian-Allen contact lens electrode (Hansen Ophthalmic Development Laboratory, Iowa City, IA), according to International Society for Clinical

TABLE 1. Summary of Retinal Functional and Structural Testing

Subject	Age	Age at Onset	BCVA	GVF	Foveal Threshold	Color	OCT Foveal Thickness	Rod ERG b-Wave Amplitude*	Rod ERG b-Wave Timing† (msec)	Cone ERG Flicker Amplitude‡	Cone Flicker Timing§ (msec)	mfERG	Cone Spacing Mean Z-Score	T8993C Mutant Heteroplasmy in Blood‖	T8993C Mutant Heteroplasmy in Hair Follicles‖
I-1	48	34	20/50	Dense paracentral scotoma	27 dB	6 crossing errors, tritan axis of confusion	74 μm	57	103.5	42	36.5	Severe reduction centrally	6.37	78	87
II-1	28	12	5/125	Large dense central scotoma	Not done (unstable fixation)	Not able	Not done (unstable fixation)	29	102.5	25	35.9	Not done (unstable fixation)	Not done	78	99
II-2	26	None	20/16	Full	38 dB	No errors	141 μm	70	86.5	83	28.6	Normal	−0.09	42	54
II-3	22	18	20/25	Slight constriction, 14e target	35 dB	1 crossing error, tritan axis	82 μm	22	99.5	22	33.7	Moderate reduction centrally	6.92	95	99
II-4	16	10	20/50	Constriction to 20° centrally	32 dB	2 crossing errors, tritan axis	99 μm	39	102.5	46	35.1	Severe reduction centrally	6.36	92	99

* Expressed as a percentage of the normal mean amplitude (272 μV). 2 SD below normal is 65% for rod b-wave.
‡ Expressed as a percentage of the normal mean amplitude (121 μV). 2 SD below normal is 54% for cone flicker.
† Normal rod timing is <105 msec.
§ Normal cone flicker timing is <32 msec.
‖ The degree of T8993C mutant heteroplasmy is expressed as percent of total mitochondrial DNA.

TABLE 2. Summary of Neurologic Studies

Subject	Age	Motor Exam	Sensory Exam	Reflexes	Cerebellar Exam	Neuropsychiatric Evaluation	Nerve Conduction Studies*	T8993C Mutant Heteroplasmy† in Blood; Hair
I-1	48	Moderate proximal muscle weakness and superimposed right sided pyramidal weakness	Prolonged vibratory thresholds, decreased pain sensation on right side of body	Absent triceps and ankle reflexes with no response on Babinski testing	Normal	Depression and visuospatial deficits	Mild length-dependent sensorimotor neuropathy	78; 87
II-1	28	Moderate proximal muscle weakness, subtle lower extremity spasticity	Sensory drift, prolonged vibratory thresholds in right arm, absent ankle reflexes	Brisk at knees, absent ankle reflexes	Limb ataxia	Depression	Moderate length-dependent sensory neuropathy	78; 99
II-2	26	Normal	Normal	Normal	Normal	Prior depression, slow visuospatial processing, low normal planning/ executive function	Not tested	42; 54
II-3	22	Proximal muscle weakness with superimposed pyramidal weakness especially in the lower extremities with spasticity	Prolonged vibratory thresholds, decreased pain sensation in left hand and foot	Very brisk at triceps and knees (left greater than right) and absent at ankles	Limb and truncal ataxia, sustained end gaze nystagmus and overshoot saccades, cerebellar dysarthria	Depression, poor attention, disinhibition, severely impaired visuospatial memory and verbal fluency	Moderate length-dependent sensorimotor axonal poly-neuropathy (upper and lower extremities)	95; 99
II-4	16	Mild proximal muscle weakness, lingual dysarthria	Prolonged vibratory thresholds	Reduced ankle reflexes	Limb ataxia	Impaired visuospatial memory and verbal recall	Moderate length-dependent sensorimotor axonal neuropathy (lower extremities)	92; 99

Pyramidal weakness, injury to descending motor inputs from the central nervous system; dysarthria, impairment of speech.

* Nerve conduction studies include techniques for assessing electrophysiologic evidence of peripheral nerve dysfunction.

† The degree of T8993C mutant heteroplasmy is expressed as percent of total mitochondrial DNA.

Electrophysiology and Vision (ISCEV) standards.[39] Briefly, full-field electroretinogram responses were elicited with 10-μs white light flashes and were recorded with a visual electrodiagnostic system (UTAS-E 3000; LKC technologies, Inc., Gaithersburg, MD). Five rod-mediated responses to -2.4 log cd-s/m^2 stimuli with an interstimulus interval of 10 seconds were computer averaged. Three mixed rod- and cone-mediated scotopic responses were recorded to a standard flash of $+0.4$ log cd-s/m^2 with an interstimulus interval of 30 seconds. Patients were then light-adapted to a 30 cd/m^2 background light for 10 minutes, and photopic responses were elicited with $+0.4$ log cd-s/m^2 stimuli presented at 2 Hz. Responses to 10 successive flashes were averaged. Responses were amplified at a gain of 4000, filtered between 0.3 and 500 Hz and digitized at a rate of 2000 Hz on two channels. Reduced amplitudes were reported as percent below the mean; mean values and standard deviations are presented in Table 1. Multifocal (mf)ERG testing was performed in a light-adapted state (VERIS 5.1.10X; Electro-Diagnostic Imaging, Inc., Redwood City, CA), using a Burian-Allen contact lens electrode, following ISCEV standards, as previously described.[37,38] Fundus guided microperimetry (MP-1; Nidek Technologies America Inc., Greensboro, NC) tested 45 locations within the central 8° visual field, as previously described.[37,38] Numeric sensitivities in decibels were exported and overlaid with AOSLO images (Matlab; The MathWorks, Natick, MA). Mean normal values $\pm$ 1 SD across the central 10° for subjects aged 0 to 20 years were 19.9 $\pm$ 0.4 dB, and for subjects aged 21 to 40 years were 19.5 $\pm$ 1.1 dB (Midena et al., *IOVS* 2006;47:ARVO E-Abstract 5349).

AOSLO Image Acquisition and Cone Spacing Analysis

High-resolution images were obtained using AOSLO in four subjects with stable fixation and images were analyzed using customized software to determine cone spacing measures using previously described methods.[30,37,38] Cone spacing measures were compared with 18 age-similar normal subjects ranging in age from 20 to 60 years. Cone spacing was measured at a range of eccentricities from as close to the fovea as possible out to 5° eccentricity in all directions. The average number of measurements per subject was just over eight, with no more than 12 measures for any one individual. An exponential function was fit to the spacing:

$$\text{Cone spacing} = Ae^{(-B\times\text{eccentricity})} + C$$

where A, B, and C are constants. Confidence intervals (95%) were estimated using the Matlab curve fitting toolbox (The MathWorks). The *z*-score for each cone-spacing measurement for the NARP patients was computed as the number of standard deviations from the best-fitting line to the normal data.

To further quantify the differences between the patients, we performed a Voronoi analysis of selected cones in each of the subjects imaged with AOSLO, and generated metrics similar to those reported previously on photoreceptor mosaics.[40–43] Contiguous sets of at least 100 cones were selected in two regions, one at or close to the fovea and a second at approximately 1° in the temporal direction. The exact locations varied depending on where unambiguous, contiguous arrays of cones were best visualized. The SD of the Voronoi domain areas of the selected cones and the percentage of triangularly packed cones were the main metrics used for comparison.

Genetic Testing

Whole blood samples were obtained for DNA extraction and PCR amplification of mtDNA (Athena Diagnostics, Worcester, MA). Direct detection of T8993C mutation was performed by restriction endonuclease digestion of PCR amplified mtDNA, followed by agarose gel electrophoresis.

Since significant variation in tissue mutant load may occur in individuals with mtDNA 8993 mutation, real-time allele refractory mutation system (ARMS) quantitative (q)PCR analysis was performed on DNA samples from hair bulbs (derived from ectoderm) and blood leukocytes (derived from mesoderm).[11] Mutant load expressed in hair bulbs may reflect brain mutant load, and similarly may reflect photoreceptor mutant load.[11] Total DNA was extracted from peripheral blood samples and a pool of 20 hair bulbs sampled from three different scalp locations, according to published procedures.[44,45]

Detection and Quantification of Mutant Heteroplasmy

Heteroplasmic mutation was confirmed by PCR/ASO (allele specific oligonucleotide) dot blot analyses and quantified with real-time ARMS-qPCR.[46] The primers for real-time ARMS qPCR assay were ARMS-T8993-1m: 5′TACTCATTCAACCAATAGCCaT3′, ARMS-T8993C-1m: 5′TACTCATTCAACCAATAGCCaC3′, and reverse primer mtR9046: 5′TTAGGTGCATGAGTAGGTGGC-3′. The lowercase nucleotide "a" indicates a mismatch. The same reverse primer was used for the amplification of both mutant and wild-type mtDNA. Samples containing various heteroplasmic concentrations of the T8993C mutation (generated by mixing the plasmid DNA containing wild-type (T8993) and mutant (T8993C) sequences) were included in each run to ensure the reliability of the assay. The T8993C mutant load concentration in these samples was 0%, 25%, 60%, 75%, 90%, 95%, and 100%.

Results

Family Members with Neurologic and Retinal Disease

The pedigree is shown in Figure 1. Subjects I-1, II-1, II-2, II-3, and II-4 were studied. A brother of I-1 had coordination problems, and a maternal aunt of I-1 gave birth to four children (two males, two females) who died in infancy due to unknown causes. Subject I-1 traces her lineage back to Colombia, with a history of immigration from Spain.

Clinical Examination

Visual and retinal findings in the study eye of each subject are presented quantitatively in detail in Table 1. Neurologic findings are detailed in Table 2.

The fundus examination in subject I-1 showed attenuated vessels, mid-peripheral bone spicule pigment with RPE atrophy along the retinal vascular arcades, and a preserved island of RPE cells at the fovea in each eye (left eye shown in Fig. 2A). The left eye was chosen as the study eye. Goldmann visual field (GVF) testing revealed a dense paracentral scotoma (Fig. 2B). The foveal threshold (measured using the Humphrey Visual Field Analyzer as described in the Methods section) was abnormal at 27 dB. Fundus-guided microperimetry showed loss of at least two log units sensitivity beginning at 2° eccentric to fixation; centrally, sensitivities were at least one log unit lower than normal (Fig. 2C). Full-field ERG cone-mediated amplitudes were reduced to a greater extent than mixed rod- and cone-mediated or rod-mediated amplitudes; rod-mediated implicit times were normal, whereas mixed responses were delayed by 8.5 ms (msec); cone-mediated implicit times were delayed by 4.5 msec to a flicker stimulus. Multifocal ERG responses were severely reduced throughout the central macula, with a small response measurable at the fovea. An OCT scan through fixation showed thin outer nuclear layer (ONL) and photoreceptor inner segment layer (ISL) and outer segment layer (OSL) with attenuation of the RPE layer throughout the macula, with a small abnormal, but somewhat better-preserved, region at the fovea (Fig. 3C). Neurologic examination revealed modest proximal muscle weakness and mild length-dependent sensorimotor neuropathy, defined as a primary axonal neuropathy affecting distal nerves first, and then affecting more proximal nerves; there was no ataxia or major cognitive dysfunction.

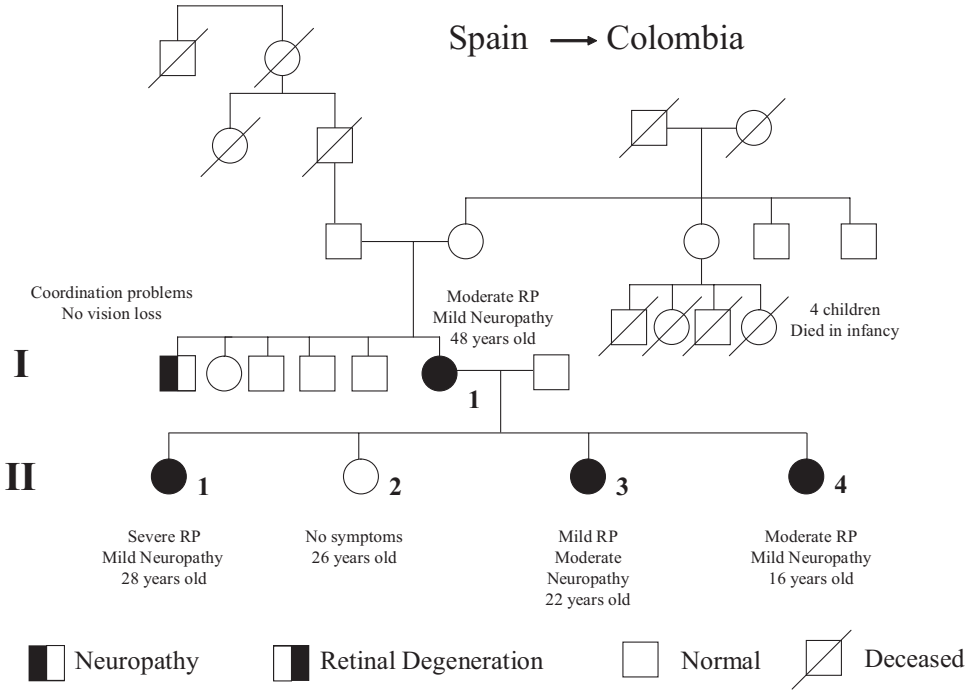

FIGURE 1. Family Pedigree. *Squares* indicate males, *circles* indicate females. *Filled symbols* on the *left half* indicate neuropathy while *filled symbols* on the *right half* indicate retinopathy. *Diagonal lines* indicate deceased individuals. Examined individuals are indicated numerically (I-1, II-1, II-2, II-3, II-4) as in the text.

Visual acuity was severely reduced in subject II-1 to 5/125 (13 letters at 1 meter) in the right eye and counting fingers at two feet in the left; examination revealed extensive bone spicule pigmentation and optic nerve pallor in each eye. GVF testing showed a dense central scotoma extending to 20° nasally and to 50° temporally, with inability to see the I-4e

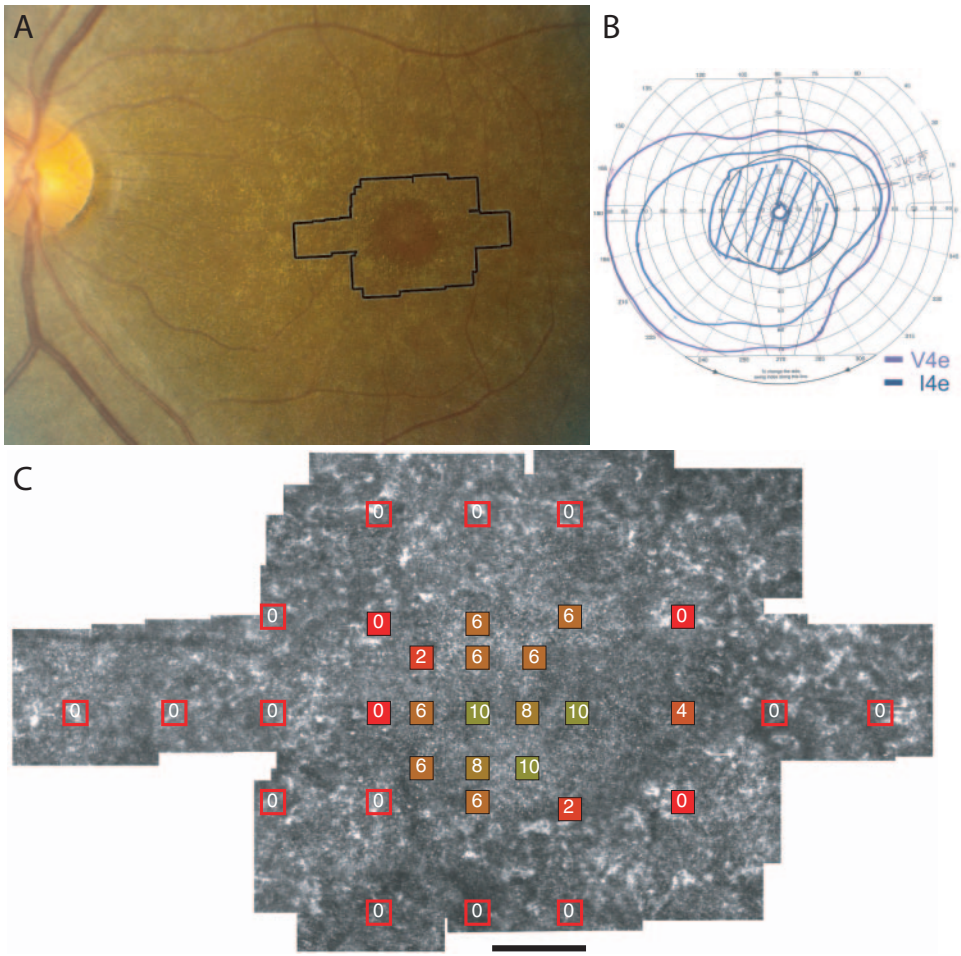

FIGURE 2. The cone receptor mosaic was imaged using AOSLO in the region outlined on the fundus photograph belonging to subject I-1, showing RPE mottling surrounding a small central island of preserved RPE (**A**); GVF testing showed a dense pericentral scotoma to the V4e and I4e targets with a preserved central island corresponding to the preserved RPE seen on examination (**B**); AOSLO images showed increased cone spacing with patchy cone loss, with corresponding absolute scotomas (indicated as 0) shown with superimposed microperimetry results (**C**). Scale bar, 1°.

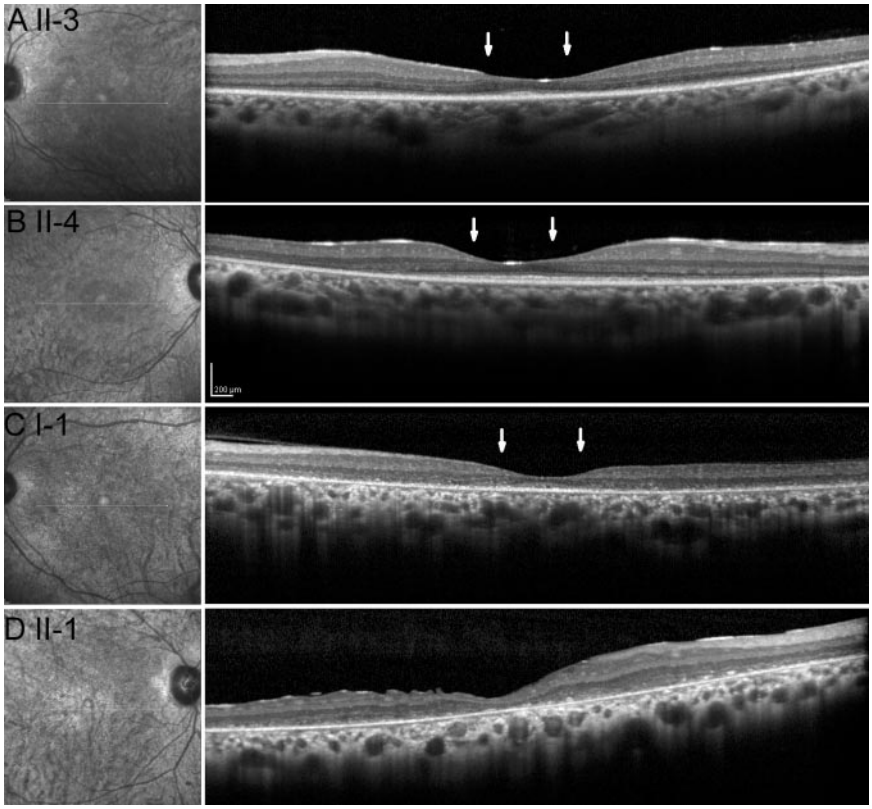

FIGURE 3. OCT images of four of the subjects. The OCT scans are 20° horizontal scans across the retina including the foveal center. IR fundus images with the scan line indicated are shown on the *left*. *Arrows* indicate the extent of the AOSLO images shown in Figure 4 for subjects II-3, II-4, and I-1. (**A**) In subject II-3, a central region of preserved photoreceptor outer nuclear layer (ONL), inner segment layer (ISL), and outer segment layer (OSL) extends to approximately 2° eccentricity in all directions, while a ring of approximately 1° width between 2° to 3° shows loss of the ONL, ISL, and OSL. More normal outer retinal structure is restored at 3° in all directions. Subject II-4 (**B**) shows preserved outer retinal structure at the fovea with progressive attenuation of the ONL, ISL, and OSL beginning gradually around 5° eccentric to fixation and extending throughout the region imaged. Subject I-1 (**C**) shows more abrupt loss of the ONL, ISL, and OSL beginning within 1° from a preserved region at the fovea. (**D**) An external fixation target was used to align the scan with the foveal center in subject II-1. The OCT shows complete loss of the ONL, ISL, and OSL with disruption of the RPE layer throughout the region imaged, including the foveal center.

target OU. Full-field ERG rod-mediated, mixed, and cone-mediated amplitudes were severely reduced by more than two standard deviations from the mean, and all responses showed delayed timing. Unstable fixation prevented reliable automated visual field, color, or mfERG testing and AOSLO images were not obtained. However, OCT images showed loss of the ONL and photoreceptor ISL and OSL, with disruption of the RPE layer throughout the macula (Fig. 3D). Neurologic examination revealed moderate muscle weakness affecting proximal to a greater extent than distal muscles, ataxia, and moderate length-dependent sensory neuropathy.

In subject II-2, the ocular examination and all visual function tests were normal in each eye. The right eye was selected as the study eye. Neurologic examination was entirely normal.

Subject II-3 showed slightly reduced visual acuity of 20/25 with retinal vascular attenuation in each eye. GVFs were mildly constricted to the I-4e target only. The left eye was chosen as the study eye. The foveal threshold was normal at 35 dB. Fundus-guided microperimetry showed a ring of sensitivity loss between 1 to 1.5 log units from approximately 2° to 3° eccentric to fixation, with improved function from 3° to 4° eccentricity where sensitivity was within 0.5 log unit of normal. Full-field ERG amplitudes were reduced by more than 2 SD from the mean, with delayed timing to all stimuli. Multifocal ERG testing revealed moderate reduction throughout the macula, with a preserved response at the central trace. An OCT scan through the fovea showed a central region of preserved outer retinal structure, with thinning of the photoreceptor ONL and loss of the ISL and OSL beginning at 2° eccentric to fixation in all directions (Fig. 3A), corresponding to regions of reduced sensitivity observed on fundus-guided microperimetry. However, peripheral to 3°, outer retinal structure was more normal. Neurologic examination showed mild cognitive impairment with modest cerebellar dysfunction, including sustained end-gaze nystagmus, overshoot saccades, mild cerebellar dysarthria, and limb ataxia. Subject II-3 also had proximal muscle weakness with superimposed pyramidal weakness, especially involving the lower extremities. Nerve conduction studies and electromyography revealed a symmetric, length-dependent sensorimotor axonal polyneuropathy.

Subject II-4 showed moderately reduced visual acuity of 20/50 in both eyes. Fundus examination revealed attenuated vessels, peripheral RPE mottling, and rare bone spicule pigment in each eye. The right eye was chosen for further study. GVF testing showed severe constriction to 20° centrally. The foveal threshold was abnormal at 32 dB. Fundus-guided microperimetry showed somewhat patchy loss of sensitivity of 1 to 2 log units within the central 8°. Full-field ERG amplitudes were all reduced by greater than 2 SD below the mean and all responses showed delayed timing. Multifocal ERG responses

were severely reduced throughout the macula. An OCT scan through the fovea showed progressive attenuation of the photoreceptor ISL and OSL beginning approximately 2° eccentric to fixation with a preserved region at the fovea (Fig. 3B). Neurologic examination revealed modest cerebellar dysfunction. Symmetric length-dependent sensorimotor axonal neuropathy was confined to the lower extremities.

Variability in Cone Spacing within and between Subjects

High-resolution photoreceptor mosaic images were obtained using AOSLO in subjects I-1, II-2, II-3, and II-4 (fixation was not stable enough for image acquisition in subject II-1). Regions of increased cone spacing correlated with reduced sensitivities measured with fundus-guided microperimetry in all subjects (i.e., subject I-1 shown in Fig. 2C). Three distinct cone mosaic patterns were observed among the four subjects. The asymptomatic subject II-2 showed entirely normal cone spacing throughout the central 4° of retina (pattern 1, Fig. 4A). Pattern 2 was characterized by contiguous and regular mosaics of cones with increased cone spacing which increased with eccentricity from the fovea, while pattern 3 showed patchy cone loss with cone spacing that was increased uniformly across the central macular region studied. Subject II-3, with the most severe neurologic dysfunction and mild to moderate retinal dysfunction, demonstrated a contiguous and regularly spaced array of preserved cones across the central 3° with uniformly increased cone spacing with eccentricity from the foveal center (pattern 2, Fig. 4B). Cones at the foveal center were easily resolved and were larger than normal. A distinct ring at approximately 0.5° eccentricity showed dimly visible cones. Outside this ring, cone packing was contiguous and cone spacing increased with eccentricity, but cone spacing was much greater than normal, exceeding that of I-1 and II-4 outside 1°. Pattern 3 was distinguished by moderate retinal dysfunction and patchy regions of increased cone spacing with cone loss (subjects II-4 and I-1; Figs. 4C, 4D). Unlike the contiguous mosaic of cones with increased cone spacing seen in pattern 2, in pattern 3 very few regions contained contiguous arrays of cones, but cone spacing was closer to normal than in pattern 2, where contiguous mosaics were present. In addition, in pattern 3 cone spacing was nearly uniform across the central macular region imaged. There was little increase in cone spacing with eccentricity as observed in normal subjects and in pattern 2. The visibility of the cone mosaic was correlated with the regions where intact photoreceptor layers were seen on OCT scans. The most contiguous regions were selected for quantitative cone spacing analysis. As such, the cone spacing reflects the average separation between cones in the most preserved areas but should not be used to infer cone density. Cone density is a meaningful correlate of cone spacing only if cone packing is uniform. Since cone spacing measures were possible only in regions where unambiguous cones were observed, the patchy regions of cone loss that characterize pattern 3 make quantification of cone spacing an inappropriate measure of cone density. Figure 5A shows the relationship between cone spacing measures and retinal eccentricity. Subject II-2 fell within the normal range at all eccentricities. Subject II-3 showed abnormally increased cone spacing that increased with eccentricity from the fovea. Subjects I-1 and II-4 showed abnormally increased cone spacing with no predictable relationship to retinal eccentricity. Average *z*-scores (number of standard deviations from normal) for cone spacing within 2° of fixation were as follows: subject I-1: 6.37; II-2: −0.09; II-3: 6.92; and II-4: 6.36.

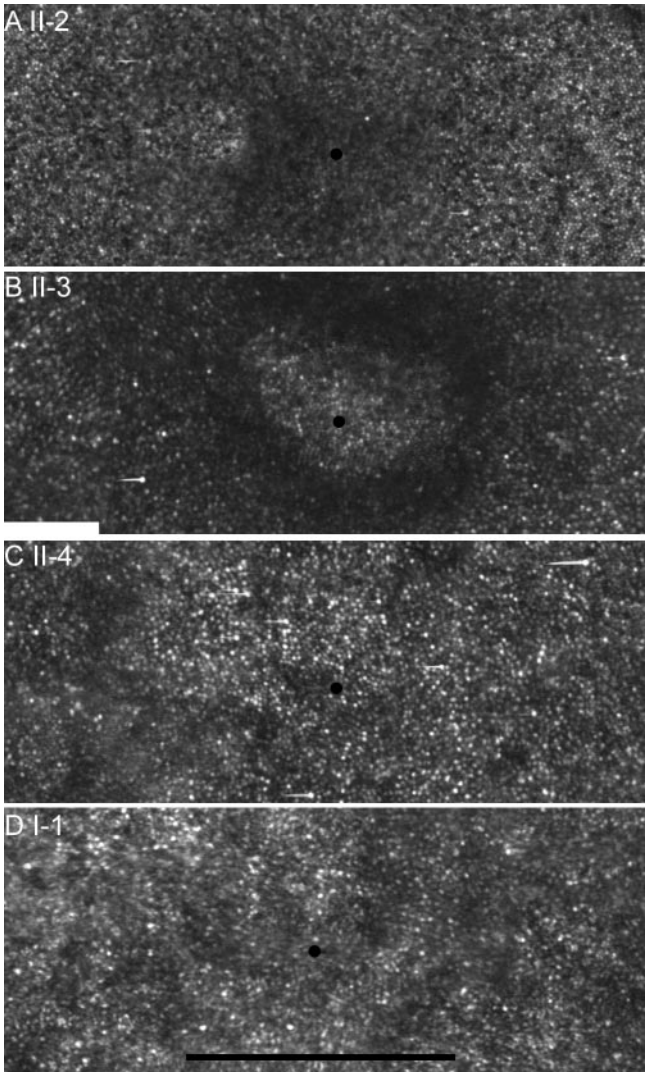

FIGURE 4. Comparison of cone structure near the fovea in patients with T8993C mutations. The *small black dot* in each image indicates the preferred fixation point. All images are to the same scale. (**A**) Subject II-2 has normal cone spacing at all eccentricities (cones within 0.5° of the foveal center are often difficult to resolve in this and other normal subjects). (**B**) Subject II-3 shows coarse cones with increased cone spacing at the foveal center, surrounded by a ring where cones are only dimly visible. A contiguous array of cones peripheral to this ring is visualized, although cone spacing is increased. Subjects II-4 (**C**) and I-1 (**D**) show similar patterns of sparse cones with increased cone spacing near fixation. Peripheral to regions of preserved cones are regions where unambiguous cones cannot be seen. (**D**) represents the central 2.5° of the image shown in Figure 2C. Scale bar, 1°.

Voronoi Analysis

Table 3 reports the location, average Voronoi area, SD of Voronoi area in percentage (which normalizes that metric against cone spacing differences), and percentage of six-sided Voronoi polygons. Smaller standard deviations indicate cones that are more regularly packed. A higher percentage of six-sided Voronoi polygons indicates that the packing is triangular. In agreement with the qualitative reports above, the normal appearing retina of subject II-2 had the lowest SD, the smallest average Voronoi area for each location, and the largest number of six-sided polygons. II-2's packing statistics are comparable to those obtained in other studies of normal eyes at a similar location.[40,42] The cones at II-2's foveal center were not re-

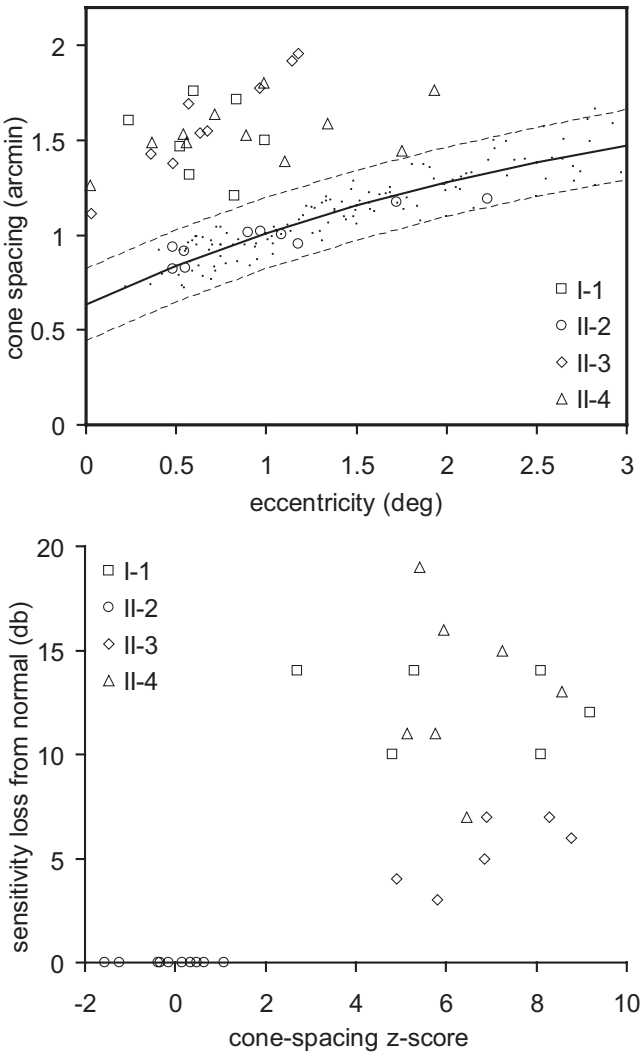

FIGURE 5. **(A)** Cone spacing of NARP patients and normal subjects versus eccentricity. Data from the normal subjects are plotted as small *dots*. *Solid line*: best fit to normal data. *Dashed lines*: 95% confidence limits of the best fit. Subject II-2 shows normal cone spacing, but all others show increased spacing. **(B)** Plots of fundus-guided microperimetry sensitivity loss in decibels versus cone spacing *z*-scores reveal the functional consequences of patchy cone loss (see Fig. 3) on visual performance. Subject II-3 performs better than subjects I-1 and II-4, likely due to the presence of a contiguous cone mosaic.

solved, so we measured cones at the closest possible location. The next most regularly packed mosaic—according to SD and percentage of six-sided polygons—was from subject II-3, although the Voronoi areas were significantly larger. Subjects I-1 and II-4, both of whom exhibited the same pattern, had similar statistics. They had the highest SD, and the lowest percentage of triangularly packed cones. In addition, they showed the smallest relative increase in Voronoi areas between the fovea and the eccentric location.

Structure-Function Correlation

Figure 5B shows the relationship between microperimetry values and cone spacing expressed as *z*-scores. Subject II-2 had normal sensitivity and cone spacing. Subject II-3 showed increased cone spacing with visual sensitivity losses of 0.5 to 1 log unit compared to normal. Subjects I-1 and II-4 showed regional variation in cone spacing with patchy cone loss and severe visual sensitivity losses of 1 to 2 log units compared to normal. Given that standard deviations from normal mean sensitivity values are <1.1 dB, the sensitivity losses observed in subjects I-1 and II-4 are greater than four standard deviations from normal.

Genetic Testing

The T8993C mutation in the ATP synthase 6 gene of the mitochondrial genome was identified in all subjects. DNA samples from blood and hair follicles were analyzed for mutant heteroplasmy (Table 1). The mutant loads ranged from 87% to 99% (I-1, II-1, II-3, and II-4) in hair follicles, and varied between 78% (I-1 and II-1) to 99% (II-3 and II-4) in blood from symptomatic subjects. The asymptomatic subject (II-2) had mutant loads ranging from 34.1% to 86.6% in hair follicles, with an average of 54%, and moderate levels in blood (42%).

DISCUSSION

We have characterized retinal structure at the individual photoreceptor level using AOSLO images in four members of a family with NARP carrying the mtDNA T8993C mutation. Despite similar high levels of mutant heteroplasmy, subjects showed significant interindividual and intraretinal variability in disease expression.

Three patterns of cone spacing were seen in the subjects with fixation stable enough to obtain high-resolution cone images. Pattern 1 was entirely normal throughout the central 4° eccentric to the fovea, and was associated with normal vision in subject II-2 with relatively low T8993C mutant heteroplasmy. Pattern 2 showed increased cone spacing and moderate disorder within a contiguous cone mosaic, and was associated with mild visual abnormalities in subject II-3, with high mutant heteroplasmy and severe neurologic abnormalities. This pattern included a ring at 0.5° eccentricity where unambiguous cones were only dimly visualized. Visual function was not measurably reduced in association with this ring; this is not surprising given the limited sampling resolution of the microperimetry technique used, with a Goldmann size III target subtending 26 arc minutes (~0.5°). Pattern 3 showed increased cone spacing with patchy cone loss. The two subjects with this pattern, I-1 and II-4, had the most significant visual dysfunction. Although these observations represent a very small number of patients, taken together, the results suggest that a contiguous and ordered cone mosaic is important for mediating suitably measurable visual function, despite increased cone spacing within that mosaic.

These findings represent the first direct visualization of neurons with high levels of mtDNA T8993C mutant hetero-

TABLE 3. Results from Voronoi Analysis of the Cone Mosaic for Four Patients Imaged with AOSLO

Patient	Location	Voronoi Area Average (arcmin^2)	Voronoi Area SD (%)	% of 6-Sided Voronoi Polygons
I-1	0.2 deg T	1.56	21.6	41
	0.94 deg T	1.83	25.0	40
II-2	0.68 deg T	0.71	11.6	76
	0.97 deg T	0.85	9.7	69
II-3	0.14 deg IT	1.09	11.3	53
	1.12 deg T	3.18	18.1	54
II-4	0.16 deg S	1.41	16.3	40
	1.3 deg T	1.70	23.9	34

T, temporal to fixation; IT, inferotemporal to fixation; S, superior to fixation; deg, degrees.

plasmy in living patients. The regional variability observed in pattern 3 may be due to variation in levels of mutant load between individual cones or between underlying RPE cells, or due to local differences in environment such as macular pigment or RPE cell pigment. Further study of these subjects over time should provide insight into patterns and rates of macular cone loss in patients with the T8993C mutation.

The levels of mutant heteroplasmy and associated clinical phenotype of patients with T8993C mutation can vary substantially.[9,10,13,20,47] The mutant load in hair follicles presumably reflects mutant load in other ectodermally-derived tissues, such as the photoreceptors and the brain, in which mtDNA cannot be quantified readily.[11] Symptomatic individuals in the present study had high mutant loads in hair follicles (mean, 87% to 99%). All subjects had relatively good neurologic function, in contrast to a severely affected pedigree in which high T8993C mutant load was associated with Leigh syndrome.[13] The asymptomatic subject (II-2) showed much lower mutant load in hair follicles (54%) than the symptomatic subjects. In general, mutant load is proportional to disease severity in affected tissues, although age and duration of disease may also be related to phenotype severity.

Direct visualization of affected cones at the cellular level may provide insight into the mechanisms of vision loss in patients with mtDNA mutations. Cone photoreceptor inner segments, key optical elements in the waveguiding portion of cone photoreceptors, contain abundant mitochondria. AOSLO images provide an in vivo look at neurons containing high levels of mitochondria expressing the T8993C mutation. Our images demonstrate not only patchy loss of visible cones as observed in pattern 3, but also abnormal waveguiding properties of individual cones, as observed by the dark perifoveal ring seen in pattern 2. Based on the localized regional losses of visual sensitivity observed using microperimetry that correlate with regions of increased cone spacing observed using AOSLO, cones expressing high levels of mitochondrial DNA mutation T8993C have altered waveguiding characteristics that impair normal visual function. These findings suggest that intact mitochondria in cone inner segments are necessary for normal optical function, which may contribute to vision loss independently of cone death.

The increased cone spacing we observed in subjects I-1, II-3, and II-4 may reflect cone loss due to degeneration or abnormalities of cone inner segment structure associated with the T8993C mutation. Surviving cones may be swollen due to increased size of the mitochondria expressing this mutation. Although a single study reporting electron micrographic characteristics of an eye expressing the more severe T8993G mutation did not demonstrate swelling of photoreceptors, swelling was observed in nonpigmented ciliary epithelium and retinal pigment epithelial cells.[25] In addition, some authors have suggested that the mitochondria in patients with other types of mitochondrial disease may proliferate to compensate for metabolic deficiency.[48] A similar phenomenon may have occurred in our patients, resulting in the increased cone spacing we observed.

A characteristic feature of mitochondrial mutations is variability in disease expression between cells expressing different levels of the mitochondrial mutation. In this family, we observed three distinct patterns in four subjects, demonstrating significant interindividual and intraretinal variability. Subjects I-1 and II-4 had patchy, irregular cone mosaics with increased spacing across the central 2° to 3°, whereas subject II-3 had increased cone spacing, but had a regular and contiguous mosaic that increased in spacing with eccentricity. In fact, subject II-3 had the greatest cone spacing (most cone loss) at 1°, the most eccentric location that we could measure in her eye. This subject had the least severe retinal dysfunction and has experienced little progressive retinal degeneration since the subject's diagnosis by ERG performed elsewhere 11 years ago, although she has had severe progressive neurologic dysfunction. A possible explanation for the appearance for subject II-3's mosaic is that the mitochondrial mutation affected her cones earlier, perhaps during early development, leaving time for the remaining cones to migrate into a regular mosaic with little progressive cone degeneration. By contrast, a progressive or later-onset degeneration is predicted to leave holes and gaps in the mosaic, as was observed in subjects I-1 and II-4, both of whom reported subjective progressive loss of night vision and visual acuity since their diagnosis 11 years ago. Carroll and associates reported a case in which a subset of cones in an individual degenerated after retinal development and foveal cone migration, leaving a closely packed, but incomplete mosaic.[34] By contrast, blue cone monochromat carriers, who experience degeneration of a subset of cones at a very early stage, have a nearly contiguous and closely packed mosaic with decreased density (Carroll J, et al., *IOVS* 2005;46:ARVO E-Abstract 4564). In neither of the previously reported cases are the remaining cones degenerating and, as a result, these eyes function normally by most measures, despite the reduced number of cones.

The 8993 mtDNA mutations cause a varied clinical phenotype between and within families, depending on mutation type, mutant loads in different tissues, and likely other unknown factors, including environment, high-demand metabolic states such as pregnancy, or nuclear genetic background.[14] Since individual neurons such as photoreceptors are not amenable to biopsy, in vivo single-cell imaging permits a unique opportunity to evaluate the effects of T8993C mtDNA mutation on these cells. High-resolution in vivo cone imaging provides a sensitive measure of the severity, type, and progression of disease in patients with mitochondrial genetic disorders affecting the retina. Repeated imaging can be used to monitor progression and treatment efficacy as treatments to slow photoreceptor degeneration become available in the future.[49]

References

1. Newman NJ. Mitochondrial disease and the eye. *Ophthalmol Clin North Am.* 1992;5:405–424.
2. Schmiedel J, Jackson S, Schafer J, Reichmann H. Mitochondrial cytopathies. *J Neurol.* 2003;250:267–277.
3. Lin MT, Beal MF. Mitochondrial dysfunction and oxidative stress in neurodegenerative diseases. *Nature.* 2006;443:787–795.
4. Mullie MA, Harding AE, Petty RK, Ikeda H, Morgan-Hughes JA, Sanders MD. The retinal manifestations of mitochondrial myopathy. A study of 22 cases. *Arch Ophthalmol.* 1985;103:1825–1830.
5. Holt IJ, Harding AE, Petty RK, Morgan-Hughes JA. A new mitochondrial disease associated with mitochondrial DNA heteroplasmy. *Am J Hum Genet.* 1990;46:428–433.
6. Tatuch Y, Christodoulou J, Feigenbaum A, et al. Heteroplasmic mtDNA mutation (T—G) at 8993 can cause Leigh disease when the percentage of abnormal mtDNA is high. *Am J Hum Genet.* 1992; 50:852–858.
7. de Vries DD, van Engelen BG, Gabreels FJ, Ruitenbeek W, van Oost BA. A second missense mutation in the mitochondrial ATPase 6 gene in Leigh's syndrome. *Ann Neurol.* 1993;34:410–412.
8. Rahman S, Blok RB, Dahl HH, et al. Leigh syndrome: clinical features and biochemical and DNA abnormalities. *Ann Neurol.* 1996;39:343–351.
9. Santorelli FM, Mak SC, Vazquez-Memije E, et al. Clinical heterogeneity associated with the mitochondrial DNA T8993C point mutation. *Pediatr Res.* 1996;39:914–917.
10. White SL, Collins VR, Wolfe R, et al. Genetic counseling and prenatal diagnosis for the mitochondrial DNA mutations at nucleotide 8993. *Am J Hum Genet.* 1999;65:474–482.

11. Enns GM, Bai RK, Beck AE, Wong LJ. Molecular-clinical correlations in a family with variable tissue mitochondrial DNA T8993G mutant load. *Mol Genet Metab.* 2006;88:364–371.
12. Makela-Bengs P, Suomalainen A, Majander A, et al. Correlation between the clinical symptoms and the proportion of mitochondrial DNA carrying the 8993 point mutation in the NARP syndrome. *Pediatr Res.* 1995;37:634–639.
13. Suzuki Y, Wada T, Sakai T, et al. Phenotypic variability in a family with a mitochondrial DNA T8993C mutation. *Pediatr Neurol.* 1998;19:283–286.
14. Debray FG, Lambert M, Lortie A, Vanasse M, Mitchell GA. Long-term outcome of Leigh syndrome caused by the NARP-T8993C mtDNA mutation. *Am J Med Genet A.* 2007;143:2046–2051.
15. Ortiz RG, Newman NJ, Shoffner JM, Kaufman AE, Koontz DA, Wallace DC. Variable retinal and neurologic manifestations in patients harboring the mitochondrial DNA 8993 mutation. *Arch Ophthalmol.* 1993;111:1525–1530.
16. Tsao CY, Mendell JR, Bartholomew D. High mitochondrial DNA T8993G mutation (<90%) without typical features of Leigh's and NARP syndromes. *J Child Neurol.* 2001;16:533–535.
17. Chowers I, Lerman-Sagie T, Elpeleg ON, Shaag A, Merin S. Cone and rod dysfunction in the NARP syndrome. *Br J Ophthalmol.* 1999;83:190–193.
18. Porto FB, Mack G, Sterboul MJ, et al. Isolated late-onset cone-rod dystrophy revealing a familial neurogenic muscle weakness, ataxia, and retinitis pigmentosa syndrome with the T8993G mitochondrial mutation. *Am J Ophthalmol.* 2001;132:935–937.
19. Uziel G, Moroni I, Lamantea E, et al. Mitochondrial disease associated with the T8993G mutation of the mitochondrial ATPase 6 gene: a clinical, biochemical, and molecular study in six families. *J Neurol Neurosurg Psychiatry.* 1997;63:16–22.
20. Sciacco M, Prelle A, D'Adda E, et al. Familial mtDNA T8993C transition causing both the NARP and the MILS phenotype in the same generation. A morphological, genetic and spectroscopic study. *J Neurol.* 2003;250:1498–1500.
21. Hogan MJ, Alvarado JA, Weddell JE. *Histology of the Human Eye*. Philadelphia, PA: W. B. Saunders Co.; 1971:687.
22. Hoang QV, Linsenmeier RA, Chung CK, Curcio CA. Photoreceptor inner segments in monkey and human retina: mitochondrial density, optics, and regional variation. *Vis Neurosci.* 2002;19:395–407.
23. Perkins GA, Ellisman MH, Fox DA. Three-dimensional analysis of mouse rod and cone mitochondrial cristae architecture: bioenergetic and functional implications. *Mol Vis.* 2003;9:60–73.
24. Perkins GA, Ellisman MH, Fox DA. The structure-function correlates of mammalian rod and cone photoreceptor mitochondria: observations and unanswered questions. *Mitochondrion.* 2004;4:695–703.
25. Hayashi N, Geraghty MT, Green WR. Ocular histopathologic study of a patient with the T 8993-G point mutation in Leigh's syndrome. *Ophthalmology.* 2000;107:1397–1402.
26. Liang J, Williams DR. Aberrations and retinal image quality of the normal human eye. *J Opt Soc Am A Opt Image Sci Vis.* 1997;14:2873–2883.
27. Liang J, Williams DR, Miller DT. Supernormal vision and high-resolution retinal imaging through adaptive optics. *J Opt Soc Am A Opt Image Sci Vis.* 1997;14:2884–2892.
28. Roorda A, Williams DR. The arrangement of the three cone classes in the living human eye. *Nature.* 1999;397:520–522.
29. Brainard DH, Roorda A, Yamauchi Y, et al. Functional consequences of the relative numbers of L and M cones. *J Opt Soc Am A Opt Image Sci Vis.* 2000;17:607–614.
30. Roorda A, Metha AB, Lennie P, Williams DR. Packing arrangement of the three cone classes in primate retina. *Vision Res.* 2001;41:1291–1306.
31. Roorda A, Williams DR. Optical fiber properties of individual human cones. *J Vision.* 2002;2:404–412.
32. Neitz J, Carroll J, Yamauchi Y, Neitz M, Williams DR. Color perception is mediated by a plastic neural mechanism that is adjustable in adults. *Neuron.* 2002;35:783–792.
33. Pallikaris A, Williams DR, Hofer H. The reflectance of single cones in the living human eye. *Invest Ophthalmol Vis Sci.* 2003;44:4580–4592.
34. Carroll J, Neitz M, Hofer H, Neitz J, Williams DR. Functional photoreceptor loss revealed with adaptive optics: an alternate cause of color blindness. *Proc Natl Acad Sci U S A.* 2004;101:8461–8466.
35. Choi SS, Doble N, Hardy JL, et al. In vivo imaging of the photoreceptor mosaic in retinal dystrophies and correlations with visual function. *Invest Ophthalmol Vis Sci.* 2006;47:2080–2092.
36. Wolfing JI, Chung M, Carroll J, Roorda A, Williams DR. High-resolution retinal imaging of cone-rod dystrophy. *Ophthalmology.* 2006;113:1019.e1.
37. Roorda A, Zhang Y, Duncan JL. High-resolution in vivo imaging of the RPE mosaic in eyes with retinal disease. *Invest Ophthalmol Vis Sci.* 2007;48:2297–2303.
38. Duncan JL, Zhang Y, Gandhi J, et al. High-resolution imaging with adaptive optics in patients with inherited retinal degeneration. *Invest Ophthalmol Vis Sci.* 2007;48:3283–3291.
39. Marmor MF, Holder GE, Seeliger MW, Yamamoto S. Standard for clinical electroretinography (2004 update). *Doc Ophthalmol.* 2004;108:107–114.
40. Baraas RC, Carroll J, Gunther KL, et al. Adaptive optics retinal imaging reveals S-cone dystrophy in tritan color-vision deficiency. *J Opt Soc Am A Opt Image Sci Vis.* 2007;24:1438–1447.
41. Galli-Resta L, Novelli E, Kryger Z, Jacobs GH, Reese BE. Modelling the mosaic organization of rod and cone photoreceptors with a minimal-spacing rule. *Eur J Neurosci.* 1999;11:1461–1469.
42. Li KY, Roorda A. Automated identification of cone photoreceptors in adaptive optics retinal images. *J Opt Soc Am A Opt Image Sci Vis.* 2007;24:1358–1363.
43. Shapiro MB, Schein SJ, de Monasterio FM. Regularity and structure of the spatial pattern of blue cones of Macaque retina. *J Am Stat Assoc.* 1985;80:803–812.
44. Lahiri DK, Nurnberger JI Jr. A rapid non-enzymatic method for the preparation of HMW DNA from blood for RFLP studies. *Nucleic Acids Res.* 1991;19:5444.
45. Wong LJ, Lam CW. Alternative, noninvasive tissues for quantitative screening of mutant mitochondrial DNA. *Clin Chem.* 1997;43:1241–1243.
46. Bai RK, Wong LJ. Detection and quantification of heteroplasmic mutant mitochondrial DNA by real-time amplification refractory mutation system quantitative PCR analysis: a single-step approach. *Clin Chem.* 2004;50:996–1001.
47. Rantamaki MT, Soini HK, Finnila SM, Majamaa K, Udd B. Adult-onset ataxia and polyneuropathy caused by mitochondrial 8993T–>C mutation. *Ann Neurol.* 2005;58:337–340.
48. Mitsumoto H, Aprille JR, Wray SH, Nemni R, Bradley WG. Chronic progressive external ophthalmoplegia (CPEO): clinical, morphologic, and biochemical studies. *Neurology.* 1983;33:452–461.
49. Sieving PA, Caruso RC, Tao W, et al. Ciliary neurotrophic factor (CNTF) for human retinal degeneration: phase I trial of CNTF delivered by encapsulated cell intraocular implants. *Proc Natl Acad Sci U S A.* 2006;103:3896–3901.